Evaluation of Variation of Permeability in Liquefiable Soil under Earthquake Loading

Hadi Shahir [a], Ali Pak [a1], Mahdi Taiebat [b], Boris Jeremić [c]

[a] *Department of Civil Engineering, Sharif University of Technology, P.O. Box 11365-9313, Tehran, Iran*

[b] *Norwegian Geotechnical Institute, P.O. Box 3930 Ullevaal Stadion, N–0806 Oslo, NORWAY*

[c] *Department of Civil and Environmental Engineering, University of California, Davis, CA 95616, USA*

Abstract

Liquefaction phenomenon is usually accompanied by large amounts of settlement owing to disruption of soil structure. In addition to that, significant settlement is also caused by a significant increase in soil permeability during seismic excitation. To properly simulate the post-liquefaction settlement, it is important to take the compressibility properties of liquefied sand as well as the permeability increase into account. Using initial permeability coefficient in simulation of liquefaction leads to underestimation of settlement. In addition to that, using unrealistic values for permeability may cause erroneous predictions of other aspects of behavior. Therefore, an accurate simulation of pore pressure generation and dissipation and consequent settlement during liquefaction requires incorporating the actual variation of permeability in the numerical model. In this paper, variation of soil permeability during liquefaction and its effects on soil seismic response is studied using a fully coupled dynamic analysis. Having a realistic mechanism for simulation of soil skeleton response using a well-calibrated critical state two-surface plasticity model, the focus of attention in this paper is on the effects of permeability variation on behavior of liquefied grounds. Numerical simulations are performed using parts of OpenSees framework, a set of coupled finite elements, constitutive integration procedures and material models from the UC Davis toolset and a novel implementation of variable permeability. Two relationships are proposed for considering the variations of permeability coefficient in the process of

[1] Corresponding author. Tel.: +98-21-66164225, Fax: +98-21-66072555, e-mail: pak@sharif.edu.

liquefaction. The proposed relationships have been implemented into the simulation system and applied for simulation of a centrifuge experiment. Comparison of the numerical results and experimental measurements reveals that there is a direct relationship between (variable) permeability coefficient and excess pore pressure ratio in all build-up, liquefaction, and dissipation phases.

Keywords: liquefaction; permeability; coupled analysis; excess pore pressure ratio

1. Introduction

The pore water pressure in loose sand deposits increases gradually under earthquake loading. This pore water pressure increase can cause a state of zero effective stress which is responsible for liquefaction phenomenon in the soil mass. Surface observation of liquefaction is usually based on land subsidence, sand boil, and lateral spreading that usually takes place during or after liquefaction.

Observations in centrifuge experiments indicate occurrence of settlement along with the initiation of earthquake loading and generation of pore pressure in the soil, suggesting that drainage of water from the soil mass is taking place during (at the same time) shaking [1]. Hence, for example, a 1D soil column under earthquake loading does not behave in a fully undrained manner, rather, generation of pore pressure and drainage of pore water occur simultaneously. During the early seconds of an earthquake, when the amplitude of seismic shaking is high, and the induced hydraulic gradient due to pore pressure generation is not significant yet, the rate of excess pore water pressure generation overcomes the drainage process (capacity), so that simple balance causes increase in pore pressure. At the same, the settlement will gradually start taking place due to drainage of water. This process continues until the pore pressure ratio becomes unity, that is until the effective stress becomes zero. At this time, the two mechanisms, that of pore pressure generation and dissipation are in balance and settlement continues to occur with the same rate. After the end of seismic excitation, the dissipation becomes dominant mechanism as the pore pressure generation ceases to supply new mass of water. At this stage, rate of settlement decreases and finally ceases completely after excess pore pressure has

been fully dissipated. It should be noted that a significant part of settlement takes place during initial process of pore pressure build-up, at the time when seismic shaking is being applied [1].

As described above, soil settlement during seismic shaking is due to the dissipation of pore water pressure/volume, and settlement will increases with the increase in the amount of generated pore pressure/volume and drainage. The main soil mechanics phenomena responsible for generation of pore water pressure/volume is the contractive soil response which subsequently leads to the obvious conclusion that more pore water pressure/volume is developed in loose deposits under earthquake loading. On the other hand, the most important parameter affecting drainage is the permeability coefficient. A large value of the permeability coefficient causes a rapid dissipation of excess pore water pressure and consequently more settlement occurs during seismic loadings. Field observations of settlement due to seismically induced liquefaction range from fractions of an inch to over a foot [2]. This large amount of settlement is due mostly to disruption of soil structure by liquefaction. Field observations and investigations show that the rate of water flow increases during liquefaction period. It has been reported in a number of investigations that one of the main mechanisms causing substantial settlement is significant increase in the soil permeability during seismic excitation [1, 3-6].

Arulanandan and Sybico [5] used Kozeny-Carman equation [7] in their study and concluded that change in the permeability coefficient during liquefaction is due to the change in pore shape factor and tortuosity. This change takes place because of reduction of contacts among sand particles, and due to soil particles beginning to float (loss of contact) in liquefied state which creates easier paths for water to flow. Based on the measurement of changes in the electrical resistance of saturated sand deposit in the centrifuge tests, Arulanandan and Sybico [5] concluded that "in-flight permeability" of saturated sand during liquefaction increases up to 6 to 7 times from its initial value.

Jafarzadeh and Yanagisawa [6] conducted a number of unidirectional shaking table tests to study the settlement of dry and saturated sand columns in various conditions. They observed that the water is expelled from the soil mass and collects top of the saturated models, due to the existence of an upward

flow along the soil column during the application of the dynamic loading. They assumed this upward flow to be laminar and employed Darcy's law for calculating the permeability coefficient during excitation. The flow rate was determined based on the volume of the expelled water in the period of applying the constant dynamic head. One of conclusion then came with was that the average permeability coefficient is 5 to 6 times greater during seismic excitation than its static (pre shaking) value.

Above described results tend to suggest that soil permeability increases significantly during pore water pressure/volume generation that comes as a consequence of seismic excitation. It appears therefore that for an accurate modeling and simulation of seismic behavior of saturated sand deposits, in addition to properly modeling compressibility properties of liquefied sand, the proper variation of permeability coefficient during liquefaction should be taken into account. It is noted that using the initial permeability coefficient in the model for simulation lead to underestimation of the amount of settlement. In addition to that, using unrealistic values for permeability may cause erroneous predictions of other aspects of behavior for the specific soil column but also in general simulation of 3D behavior of liquefied soil behavior.

Work presented in this paper utilizes a fully coupled dynamic analysis and a well calibrated constitutive model, to investigate the effects of variable soil permeability (occurring during liquefaction) on the seismic behavior of saturated sandy soils.

2. Review of liquefaction modeling considering variation of permeability

One of the major challenges in numerically simulating liquefaction phenomenon is in predicting the settlement. Numerical simulations that were conducted in the course of VELACS project [8] revealed that most of the numerical models are unable to predict the amount of settlement accurately [1].

Two factors that have significant impact on the amount of settlement in numerical modeling and simulations are:

- Constitutive model for the solid (soil skeleton) phase must be able to properly simulate contraction behavior under earthquake loading and the compressibility properties of the liquefied soil.
- Model for dissipation of pore water pressure/volume and permeability change, must be able to properly capture changes in permeability during and after earthquake loading.

Much work has been carried out on developing constitutive models that can be used for predicting proper mechanical behavior of soils, including dilation and compression response that plays crucial role in modeling of liquefaction of sands. Nevertheless, very few models have been used in the efforts on simulating effects of pore water flow on the seismic response of saturated sands. Few studies that are available are mainly focused on the effects of permeability on seismic behavior of saturated sand deposit [9], the effects of low-permeability interlayers on behavior of sand layer and redistribution of pore pressure [9-11], and variation of soil permeability during liquefaction [5, 12-14].

Assuming a "constant increased permeability coefficient" is a common method for taking the permeability variation into consideration in the process of liquefaction modeling. Arulanandan and Sybico [5] used an increased permeability coefficient, equal to $3.67k_0$ (where k_0 is the initial, static value for soil permeability), for simulation of the centrifuge experiment, during which the variation of permeability had been recorded. They obtained a good agreement between the numerical result and the experimental measurement for settlement. The value of $3.67k_0$ was used as an average value for the "initial permeability" and "in-flight permeability" and was constant during numerical simulation. Balakrishnan [12] employed an increase factor of 10 for permeability, in order to adjust the results of the numerical modeling with centrifuge measurements. Applying this factor caused the settlement to become 5 times greater and got closer to the observed value. However, this factor caused a significant reduction in the amount of peak and residual pore pressures which were far from the experimental measurements. Taiebat et al. [13] used a fully coupled effective stress numerical model with a critical

state two-surface plasticity model to simulate the VELACS model No. 1. They showed in that particular case that an increased permeability equal to 4 times of the initial value gives the best fit to the centrifuge data. However, by comparing predicted and measured short-term and long-term pore pressures, they concluded that the coefficient of permeability should not be a constant parameter during shaking and during drainage processes.

Although above described use of "constant increased permeability coefficient" in liquefaction modeling and simulations does not reflect the actual mechanics of pore water pressure/volume generation and dissipation, it is noted that it can improve the prediction of the settlement amount. However, it is clear that this assumption can not serve as a basis for rational liquefaction modeling which will lead to properly predicting (predicting in the sense of Oberkampf et al. [15]) pore pressure build-up and drainage. It is also noted that assuming ad hoc constant, increased values for permeability (in order to match experimental results) seems to disable prediction of the onset of initial liquefaction in some locations [12].

Numerical studies in which a variation in permeability has been considered are rare. For numerical simulation of VELACS model No. 1, Manzari and Arulanandan [14] used findings of Arulanandan and Sybico [5], and employed a variable permeability (as a function of time) shown in Figure 1(a). Although, the measured excess pore pressure ratios, shown in Figure 1(b), indicate that the liquefaction state was sustained for a long period during the centrifuge experiment [16], the proposed permeability function gives an increase in the permeability value only for the first seconds of liquefaction initiation. Also, in their analysis a unique permeability function was considered for all elements while different pore pressure responses were recorded along the soil column. They reported that by using their proposed permeability function, the measured settlement was simulated well. However, both rates of build-up and dissipation of pore pressure were overpredicted when compared to the experimental measurements.

The above discussions indicate that an accurate simulation of pore pressure generation and dissipation and consequent settlement during liquefaction requires incorporating the actual variation of permeability in the numerical model in addition to a suitable constitutive model for simulating contraction behavior of sand. In this paper, in addition to using a calibrated critical state two-surface plasticity model, a model was proposed for describing variation of permeability during seismic shaking induced liquefaction. Validation of the model is performed by comparison of the numerical modeling with measurements from a centrifuge experiment. In addition to that, approach using a constant increase in permeability coefficient in the analysis of liquefaction is evaluated.

3. Numerical simulation program and its formulation

Implementation of the described algorithms and procedures was performed using a number of numerical libraries. Parts of OpenSees framework [17] were used to connect the finite element domain. In particular, finite element model classes from OpenSees (namely, class abstractions for node, element, constraint, load and domain) were used to describe the finite element model and to store the results of the analysis performed on the model. In addition to these, analysis classes were used to drive the global-level finite element analysis, i.e. to form and solve the global system of equations. As for the geomechanics modules, a number of elements, algorithms and material models from UCD computational geomechanics toolset are used. In particular, a set of NewTemplate3Dep numerical libraries was used for constitutive-level integrations; nDarray numerical libraries [18, 19] were used to handle vector, matrix and tensor manipulations, whereas FEMtools element libraries were used to couple finite elements (u–p) and for element-level computations. Finally, solvers from the uMfPACK set of libraries [20] were used to solve the non-symmetric global (finite element level) system of equations.

All of the above libraries are available either through their original developers or through fourth author's web site http://geomechanics.ucdavis.edu.

For modeling of the two-phase porous medium of saturated sand, cubic eight-node elements with coupled u–p formulation has been used. The primary unknowns in this formulation are displacement of solid phase (u) and pore fluid pressure (p). The fully coupled effective stress u–p formulation is a simplified case of the general set of equations governing the behavior of saturated porous media. This formulation is applicable for dynamic problems in which high-frequency oscillations are not important, such as soil deposit under earthquake loading. Using the finite element method for spatial discretization, the u–p formulation is as follows [21]:

$$M\ddot{U} + \int_v B^T \sigma' dV - QP - f^{(s)} = 0 \tag{1a}$$

$$Q^T \dot{U} + HP + S\dot{P} - f^{(p)} = 0 \tag{1b}$$

where M is the mass matrix, U is the solid displacement vector, B is the strain-displacement matrix, σ' is the effective stress tensor, Q indicates the discrete gradient operator coupling the motion and flow equations, P is the pore pressure vector, S is the compressibility matrix, and H is the permeability matrix. The vectors $f^{(s)}$ and $f^{(p)}$ include the effects of body forces, external loads, and fluid fluxes. In Eq. (1a), which is equation of continuity of motion, the first term represents the inertia force of the mixture followed by the internal force due to soil skeleton deformation, and then by the internal force due to pore-fluid pressure. In Eq. (1b), which is the equation for continuity of fluid flow, the first and third terms represent the rate of volume change for the soil skeleton and the fluid phase, respectively, and the second term is the rate of pore fluid seepage.

4. Constitutive modeling of sand behavior

A critical state two-surface plasticity model developed by Dafalias and Manzari [22] was employed for modeling of sand behavior. A brief description of the constitutive model and the procedure of calibration of model constants are presented in the followings.

4.1. The critical state plasticity sand model

The critical state two-surface plasticity model was originally developed by Manzari and Dafalias [23] and refined later by Dafalias and Manzari [22]. The formulation of the model is based on the bounding surface plasticity theory [24] within the critical state soil mechanics framework [25] to yield a comprehensive multiaxial constitutive model for simulating monotonic and cyclic behavior of sand. A schematic representation of the two-surface model in the π-plane is shown in Figure 2. A brief description of the basic equations of the model follows.

Elastic response:

The isotropic hypoelasticity assumption is adopted with the elastic moduli, G and K, as functions of current pressure and void ratio:

$$G = G_0 p_{at} \frac{(2.97-e)^2}{1+e}\left(\frac{p}{p_{at}}\right)^{0.5} \quad ; \quad K = \frac{2(1+\nu)}{3(1-2\nu)}G \tag{2}$$

where G and K are elastic shear and bulk moduli, p is the mean effective stress, e current void ratio, ν Poisson ratio and p_{at} the atmospheric pressure.

Yield Function:

The shape of the yield surface is a circular cone with its apex at the origin, defined by:

$$f = \left[(\mathbf{s}-p\boldsymbol{\alpha}):(\mathbf{s}-p\boldsymbol{\alpha})\right]^{1/2} - \sqrt{2/3}\,mp = 0 \tag{3}$$

In the above equation $\mathbf{s}$ is the deviatoric stress tensor, m represent the size of the yield surface and the tensor $\boldsymbol{\alpha}$ determines the position of the axis of the cone. The trace of the cone on the stress ratio π-plane is a circular deviatoric yield surface with center $\boldsymbol{\alpha}$ and radius √2/3m as shown in Figure 2. The cone-type yield surface implies that only changes in the stress ratio can cause plastic deformations. In a more recent version of this family of models, Taiebat and Dafalias [26] have introduced a closed yield

surface in the form of a modified eight-curve equation with proper hardening mechanism for capturing the plastic strain under constant stress to circumvent the mentioned limitation.

Flow rule:

The increment of plastic strain tensor is given by:

$$d\boldsymbol{\varepsilon}^p = \langle L \rangle \mathbf{R} = \langle L \rangle \left(\mathbf{R}' + \frac{1}{3} D\mathbf{I} \right) \quad ; \quad \mathbf{R}' = B\mathbf{n} - C\left(\mathbf{n}^2 - \frac{1}{3}\mathbf{I} \right) \tag{4}$$

where L is the loading index enclosed by the Macauley brackets $\langle\ \rangle$ to indicate loading, unloading, or neutral loading, D dilatancy coefficient, and B and C are functions of the material state. In this equation $\mathbf{R}'$ and $D\mathbf{I}/3$ are deviatoric and volumetric parts of $\mathbf{R}$, respectively. In general, both volumetric and deviatoric parts of the flow rule are non-associated.

Based on Rowe [27], dilatancy is function of the distance from the dilatancy line in the triaxial space. This is similar to the basic idea of "distance dependency" in the bounding surface model [24]. With generalization into multiaxial space, the dilatancy coefficient is related to the distance from the dilatancy surface:

$$D = A_d \mathbf{d} : \mathbf{n} \tag{5}$$

The vector $\mathbf{d}$ shown in Figure 2, is defined as the vector connecting the current stress state to its image on the dilatancy surface. The dilatancy surface will be defined later. The positive quantity A_d was assumed a model constant in the original work by Manzari and Dafalias [23]. However, it was later observed that a constant A_d can not capture the effects of "fabric change phenomenon" arisen during stress increment reversal after a dilative plastic volumetric strain occurrence. To overcome this shortcoming, in the current model a variable A_d is adopted:

$$A_d = A_0 \left(1 + \langle \mathbf{z} : \mathbf{n} \rangle \right) \ ; \quad d\mathbf{z} = -c_z \left\langle -d\varepsilon_v^p \right\rangle \left(z_{\max} \mathbf{n} + \mathbf{z} \right) \tag{6}$$

in which $\mathbf{z}$ is the fabric-dilatancy tensor and A_0, $z_{\max}$ and c_z are positive model parameters.

Hardening law and plastic modulus:

Normally, a constant and rather small size for yield surface (m in Eq. (3)) will suffice in most applications. Thus, no isotropic hardening is considered. The evolution equation for the location, $\boldsymbol{\alpha}$, of the yield surface (i.e. kinematic hardening) are given as:

$$d\boldsymbol{\alpha} = \frac{2}{3}\langle L \rangle h \mathbf{b} \tag{7}$$

The vector $\mathbf{b}$ shown in Figure 2, is defined as the vector connecting the current stress state to its image on the bounding surface. The bounding surface will be defined later. The positive scalar-valued function h is defined based on the original proposition by Dafalias [24]:

$$h = \frac{G_0 h_0 (1 - c_h e)}{(\boldsymbol{\alpha} - \boldsymbol{\alpha}_{in}) : \mathbf{n}} \left(\frac{p}{p_{at}} \right)^{-0.5} \tag{8}$$

In this equation, h_0 and c_h are model parameters and $\boldsymbol{\alpha}_{in}$ is the value of $\boldsymbol{\alpha}$ at initiation of a loading process.

Plastic modulus is related to hardening aspects of the model. Using consistency condition, the plastic modulus is obtained based on Eq. (7) as follows:

$$K_p = \frac{2}{3} p h \mathbf{b} : \mathbf{n} \tag{9}$$

As it is seen, the plastic modulus is function of distance from the bounding surface, $\mathbf{b}$. The "distance dependent plastic modulus" is the main feature of the classic bounding surface model [24].

Critical, Bounding and Dilatancy surfaces:

In the triaxial space, the critical state of a soil [25] is attained when the stress ratio $\eta = q/p$ equals the critical value M. This indicates a straight line with the slope of M passing through the origin. In a similar way, the bounding and dilatancy lines can be introduced by defining the peak (bounding) and

dilatancy stress ratios; M^b and M^d. The line defined by M^d is the "phase transformation line" described by Ishihara et al. [28] and here named "dilatancy line". Contradictory to the critical stress ratio which is a material constant, the bounding and dilatancy stress ratios are functions of the current material state. Wood et al. [29] suggested that the bounding stress ratio can be related to the critical stress ratio by using of a linear relation. This relation was made by way of the "state parameter" [30] defined in following. Manzari and Dafalias [23] used this relation with a modification. They also made a similar proposition to relate the dilatancy stress ratio to critical stress ratio. In the modifications by Dafalias and Manzari [22], the exponential relation was adopted because of its applicability over large variations:

$$M^b = M\exp\left(-n^b\psi\right) \;;\; M^d = M\exp\left(n^d\psi\right) \tag{10}$$

where n^b and n^d are positive material constants. $\psi = e - e_c$ is the "state parameter" proposed by Been and Jefferies [30], where e is the current void ratio of the soil element and e_c is the critical void ratio corresponding to the existing confining stress.

The e_c, $\ln p$ relation, defining the Critical State Line (CSL), is usually assumed to be linear as implemented by Manzari and Dafalias [23]. However, Li and Wang [31] suggested that the power relation has a greater range of applicability for different pressures. In the current model, the power relation has been adopted for CSL as follows:

$$e_c = e_0 - \lambda_c\left(\frac{p_c}{p_{at}}\right)^{\xi} \tag{11}$$

where e_0, λ_c and ξ are critical state constants.

The generalization to the multiaxial stress space is obtained by introducing three bounding, dilatancy, and critical surfaces in direct correspondence to the bounding (peak), dilatancy, and critical stress ratios using a function of the modified Lode angle (θ). The modified Lode angle (θ) is defined in the stress ratio space as shown in Figure 2. A schematic representation of these surfaces in the stress

ratio π plane is illustrated in Figure 2. Bounding and dilatancy surfaces are shown by discontinuous lines indicating their change with ψ and the critical surface by a solid line. All surfaces are fully determined by the value of state parameter ψ and this increase the numerical efficiency of the model. Also, the state parameter includes combined effect of density (void ratio) and confining stress. Thus, one of the main features of the current constitutive model is its applicability to all densities and confining pressures with the same set of material constants.

4.2. Model constants calibration

The constants of Manzari and Dafalias [23] model were originally calibrated for Nevada sand. However, the version of the model proposed by Dafalias and Manzari [22] was calibrated using the triaxial test data on Toyoura sand. In this paper, Dafalias and Manzari [22] model is to be employed for simulation of a centrifuge experiment in which Nevada sand was used. Therefore, the model constants should be calibrated for Nevada sand. For this purpose, laboratory tests performed on Nevada sand by Earth Technology Corporation in the course of the VELACS project [32] were used. List of the model constants is shown in Table 1. The model has 15 constants divided into 6 categories based on their functions. In the following, the procedure of calibration and the relevant effects of constants are explained.

Shear modulus is the main parameter which controls the soil shear deformation in a shear loading test. Also, it affects initial slope of the $q-\varepsilon_a$ curve in a drained compression triaxial test. In addition to shear modulus, plastic modulus parameters h_0 and c_h have great influence on the curve slope. In undrained condition, the stress-strain curve slope is less affected by the above parameters and the bulk modulus plays the main role. Thus, using a trial and error procedure, elasticity and hardening constants can be obtained by matching of the model predictions to the experimental results for initial part of the stress-strain curve in monotonic shear and triaxial (drained and undrained) tests.

The critical state parameters play a very important role in accuracy of model predictions and the final state of stress, deformation, and pore pressure are greatly influenced by these parameters. The critical state parameters can be directly derived by fitting Eq. (11) to the final states of the recorded data of soil samples at the critical state in drained and undrained tests. However, it is almost impossible to uniformly reach the critical state in sand samples because of the development of shear bands at intermediate strains. Thus, determination of the critical state parameters can be done approximately. In the current calibration scheme, the CSL parameters (e_0, λ_c and ξ) were determined by fitting the power relation of Eq. (11) to the CSL proposed by Manzari and Dafalias [23] in the pressure range of 0-1600 kPa. Regarding the final stress states in monotonic tests, the critical state stress ratio in compression (M) and the ratio of extension to compression (c) were obtained 1.14 and 0.78, respectively.

The size of the yield surface (m) is usually considered a small value. In the original and modified models, the values of $0.05M$ and $0.01M$ was proposed, respectively. Here, $m = 0.02$ was considered for increasing the numerical efficiency of the model.

The n^b indirectly determines the peak deviatoric stress value in a drained compression test and it can readily be calculated from the peak stress value and relevant void ratio; or it can be obtained by trial and error procedure.

Dilatancy parameters, A_0 and n^d, have influence on the volume change in drained loading and pore pressure buildup in undrained case. These parameters can be obtained by trial and error. n^d can be directly calculated from the stress state and relevant void ratio at the start of dilation phase, as well. Different sets of dilatancy parameters may produce same volumetric strain. However, it is notable that large values of A_0 results in large dilation at the beginning of loading which is not realistic.

The fabric-dilatancy tensor $\mathbf{z}$ is activated during stress increment reversal after occurrence of a dilative plastic volumetric strain. Therefore, fabric-dilatancy constants, $z_{\max}$ and c_z, should be calibrated using the cyclic tests in which the stress ratio exceeds the dilatancy stress ratio.

4.3. Constitutive model performance

Using the calibrated model constants, model predictions for various triaxial tests under different conditions are given and the capabilities of the model are demonstrated. The values of model constants used in these simulations are presented in Table 1. As mentioned above, the laboratory tests were performed by Earth Technology Corporation in the course of the VELACS project [32].

First, a series of drained monotonic compression constant-p tests conducted on soil samples with initial relative density of about 40% and 60% under three different confining pressures of 40, 80, and 160 kPa are presented. The model simulations along with the experimental results are shown in Figures 3 and 4. Good agreement with the experimental results was achieved at both densities and for different confining pressures. The softening behavior of sand samples was well captured. It is notable that the experimental data for the case of $D_r = 40\%$ show greater dilatancy for $p = 160\,kPa$ contrary to the fact that less dilatancy should occur at higher confining pressures. The model exhibits the correct trend.

The same model constants were used to simulate an undrained compression test conducted on a sample of Nevada sand with relative density of about 40%. The model simulations along with the experimental results are shown in Figure 5. Good agreement between the results of the model and test data was achieved.

A simulation of undrained cyclic triaxial test conducted on a sample with relative density of about 40% is shown in Figure 6. The soil sample was first isotropically consolidated to a mean confinement $p = 160\ kPa$. After completion of consolidation, a compressive deviatoric stress $\left(q_0 = 21.5\ kPa\right)$ was

applied as an offset under undrained conditions prior to applying the cyclic load. Thereafter, cycles of vertical loading with the amplitude of 48 kPa and the frequency of 1.0 Hz were applied. In general, the model captures the gradual generation of excess pore pressure. The cyclic mobility phenomenon and zero effective stress condition were well simulated.

5. Proposed formulations for the variation of permeability during liquefaction

The coefficient of soil permeability depends on several factors: fluid viscosity, pore size and shape distribution, grain size and shape (fabric) distribution, void ratio, roughness of soil particles, and degree of saturation. Various empirical equations have been proposed for estimating the permeability coefficient [7, 33, 34]. Among these empirical relationships, the Kozeny-Carman equation [7] includes more parameters and predicts fairly good values for permeability coefficient of sandy soils. The Kozeny-Carman equation reads:

$$k = \frac{\gamma_f}{\mu} \frac{1}{k_0 T^2 S_0^2} \frac{e^3}{1+e} \tag{12}$$

where k is permeability coefficient, γ_f unit weight of fluid, μ fluid viscosity, k_0 pore shape factor, T tortuosity, S_0 specific surface, and e void ratio.

During shaking of a sand deposit, soil mass eventually settles and its void ratio decreases. Based on the above equation, the permeability will be reduced since void ratio decreases. However, this reduction in void ratio and its effect on permeability is not significant. Arulanandan and Sybico [5] showed that permeability will increase during liquefaction due to structural change in soil skeleton, which in turn, results in reduction of pore shape factor and tortuosity parameters. At the onset of liquefaction, soil particles lose full contact with each other and this change creates additional pathways for water, which is then able to flow easier. The creation of such new, larger flow pathways reduces the pore shape factor and tortuosity and consequently leads to an increase in permeability coefficient

(during initial phases of liquefaction). Since the basic mechanism that is involved in this increase of permeability is related to the pore pressure increase, it is seems reasonable to relate the permeability coefficient of soil to the excess pore pressure ratio (r_u) which is defined as:

$$r_u = \Delta u / \sigma'_{v0} \tag{13}$$

where Δu is the excess pore water pressure and σ'_{v0} is the initial vertical effective stress.

Development of such relationship is based on the following rationale. At the beginning of seismic excitation, no excess pore pressure has yet been developed and excess pore pressure ration r_u is equal to zero, therefore the permeability coefficient has its initial at-rest value. As seismic loading (shaking) progresses, excess pore pressures are (might be) generated and consequently the permeability coefficient increases. When excess pore pressure ratio r_u becomes unity the soil mass is in a state of complete liquefaction and the permeability attains its peak value. This trend indicates a direct relationship between the permeability coefficient and r_u during the phase of pore pressure build-up. Assuming a simple power function, this relationship can be expressed by the following equation:

$$\frac{k_b}{k_i} = 1 + (\alpha - 1) \times r_u^{\beta_1} \qquad \text{in build-up phase } (r_u < 1.0) \tag{14a}$$

where k_b is the soil permeability coefficient during pore pressure build-up, k_i is initial (at-rest) permeability coefficient before shaking and α and β_1 are positive material constants. This equation shows a gradual change of permeability up to the onset of liquefaction when the permeability becomes equal to α times of the initial permeability. Material constant β_1 on the other hand, defines the rate of permeability increase during excess pore pressure increase phase (pre-liquefaction).

The liquefied state usually persists until the end of (or past) shaking. During liquefaction phase, excess pore pressure ratio r_u remains equal to unity and the soil particles are in boiling state. At the end of seismic excitation, the excess pore pressure starts to dissipate and that dissipation proceeds until

r_u becomes equal to zero in all parts of domain. Similar to the above relationship given in Equation (14a), a direct relationship can be proposed between the permeability coefficient and excess pore pressure ratio r_u for the liquefaction and dissipation phases as follows:

$$\frac{k_l}{k_i} = \alpha \qquad \text{in liquefied state } (r_u = 1.0) \tag{14b}$$

$$\frac{k_d}{k_i} = 1 + (\alpha - 1) \times r_u^{\beta_2} \qquad \text{in dissipation phase } (r_u < 1.0) \tag{14c}$$

where k_l and k_d are permeability coefficients during liquefaction and dissipation phases, respectively. Positive material constant β_2 defines the rate of permeability reduction during dissipation phase. The rate of permeability reduction in the dissipation phase is considered to be different from the permeability rising rate during pore pressure build-up.

Equations (14a,b,c) constitute a variable permeability function in which the permeability changes with respect to excess pore pressure ratio r_u from the beginning of shaking to the end of dissipation. A schematic view of the proposed permeability function and the corresponding r_u over time is shown in Figure 7. By using above equations, different permeabilities (permeability functions) can be obtained at any desired depth according to different pore pressure responses (excess pore pressure ratios) along the soil column. It is important to note that variable permeability model defined by equations (14a,b,c) is essentially governed by the same equation, except for difference in material constants β_1 and β_2 which govern the rate of permeability increase and reduction during excess pore pressure build up and dissipation, respectively.

In addition to the above proposed models, if it is hypothesized that permeability might start decreasing before the end of full liquefaction (when $r_u = 1$) since particles might start to move and settle even if dissipation is yet to start. In that case, the peak value of permeability coefficient may not remain constant until the end of liquefied state that is permeability will start to decrease earlier (e.g.

Manzari and Arulanandan [14]). A schematic diagram representing this type of behavior is also depicted in Figure 7. The mathematical form of the permeability function in this case can be written as:

$$\frac{k}{k_i}=\begin{cases}1+(\alpha-1)\times r_u^{\beta_1} & \text{in build}-\text{up phase}\ (r_u<1.0)\\ \alpha & \text{for } t_1\le t<t_2\\ 1+(\alpha-1)\left(\dfrac{t_3-t}{t_3-t_2}\right)^{\beta_3} & \text{for } t_2\le t<t_3\\ 1.0 & \text{for } t_3\le t\end{cases} \tag{15}$$

where β_3 is a positive material constant and t represents the current time. The variable permeability during excess pore pressure build up and part of full liquefaction phases are therefore described by the same relationship as in the first model (Equation (14)), while the decrease of permeability with this model, starts earlier at time t_2, and is finished by the time t_3. This new relationship for variable permeability is depicted in Figure 7, as well. Here, t_1 is the time of onset of initial liquefaction and is determined automatically during analysis by following values of r_u. Time t_2 or Δt_{peak} is used to determine the duration of peak permeability, during liquefaction state and should be defined as a model constant. Time t_3 is another constant which specifies the end of permeability variation process.

This second variable permeability model requires therefore couple more material constants (t_2 and t_3) but allows better control of variable permeability as observed in experiments.

6. Calibration of constants of variable permeability functions using centrifuge model test

6.1. Description of centrifuge experiment

The centrifuge experiment considered here for numerical modeling was done by Gonzalez et al. [35] at Rensselaer Polytechnic Institute (RPI). This centrifuge model consisted of uniform saturated Nevada No. 120 sand which was placed in a laminar box at a relative density of 55% and topped by a steel

plate. A sketch of the laminar box and the instrumentations used for this experiment is presented in Figure 8(a). The soil deposit height was 24 meters in prototype scale. The steel plate applied a uniform prototype surcharge of 140 kPa at the soil surface. Several holes were made through the steel plate to provide drainage from the soil surface. The pore fluid used in this experiment had a viscosity 40 times greater than that of water and the model was spun up to a centrifuge acceleration of 80g. The soil column was excited horizontally at the base by 50 cycles of a sinusoidal acceleration with prototype frequency of 1.5 Hz and peak acceleration of 0.2g. The prototype time history of actual input motion is shown in Figure 9.

6.2. Numerical model features

For proper simulation of a centrifuge model test in prototype scale, it is very important to establish proper scaling relationships. In the phenomenon of liquefaction of saturated fine sands during earthquake, excess pore pressure dissipation occurs during the earthquake event. Therefore, there is two time scales in this phenomenon, i.e. time scale for dynamic event and time scale for diffusion event. If model and prototype soils and pore fluids are considered the same with only difference in the pore fluid viscosity, the time scales (ratio of model value to prototype value) for dynamic and diffusion events are as follows (see details in Wood [36]):

$$n_t^{dynamic} = \frac{1}{n} \quad ; \quad n_t^{diffusion} = \frac{n_\mu}{n^2} \tag{16}$$

where n is the centrifuge acceleration or geometric scale and n_μ is the scale of pore fluid viscosity. In the described centrifuge experiment $n = 80$ and $n_\mu = 40$ which yields:

$$n_t^{dynamic} = \frac{1}{80} \neq n_t^{diffusion} = \frac{1}{160}$$

The resulting scaling factors for dynamic time and diffusion time are different. To conduct simulation in prototype scale, it is necessary to ensure that the time scaling factor for motion is the same as that for fluid flow.

According to Taylor [37], if the soils in model and prototype have different permeabilities, the effect of different permeabilities can be taken into account by enhancing the scaling relationship for diffusion time as follows:

$$n_t^{diffusion} = \frac{n_\mu}{n^2} \times \frac{k_p}{k_m} \tag{17}$$

where k_p and k_m are soil permeability in prototype and model scales.

Based on Equations 16 and 17, if k_p/k_m is considered equal to n/n_μ, this assumption will correct the diffusion time scale and the time scales for dynamic and diffusion events will be the same. In other words, a centrifuge experiment simulates a soil deposit with a permeability coefficient of n/n_μ times larger than that of model soil.

Only if the pore fluid used in centrifuge experiments is replaced with a fluid that has viscosity n times larger than water then, the model represents appropriately the water-saturated soil in the field. Thus, in the study of a particular real liquefaction problem by centrifuge modeling, the diffusion time must be properly scaled by increasing of the fluid viscosity so that the model test data can be straightforwardly extrapolated to the prototype scale and give a sensible assessment of the behavior. If the diffusion time scaling is not fulfilled in model test, this experiment can only be used for the study of a general problem with no particular prototype in mind. The main aim of these experiments is to validate a numerical program and not to model any real behavior.

In this paper, the calibration of the constants of permeability functions, which represent a real phenomenon, is to be carried out using simulation of a centrifuge model test. Therefore, it is of great importance that the centrifuge experiment replicate sufficient of the essential features of the real

phenomenon. In the chosen centrifuge experiment, there is small difference between the time scales and it can be supposed that the experimental results would more closely model prototype situation.

Based on the above discussion, to conduct the simulation of the described centrifuge experiment in prototype scale, the permeability coefficient in numerical model was considered to be twice that of Nevada sand. Preliminary simulation of the centrifuge experiment in both model and prototype scales revealed that by this assumption, exactly the same results are obtained in these two approaches.

Reported data by Gonzalez et al. [35] shows that the recorded pore pressure time histories at the same elevations within model box are essentially identical. This indicates the one-dimensional behavior of the model. Therefore, a one-dimensional finite element mesh with 22 cubic elements was used in the analyses as shown in Figure 8(b). To consider the effect of a laminar box in numerical simulation, the lateral nodes were tied together in horizontal direction (master-slave connection). It was assumed that the drainage from the soil surface was not prevented by the plate and full dissipation of pore pressure was allowed through the surface of sand layer. The plate was modeled by a rigid brick element tied to the upper soil element.

Extensive data about the characteristics of Nevada sand has been reported by Arulmoli et al. [32] in the course of VELACS project. In Table 2 the results of constant head permeability tests for different relative densities of sand are presented. From this table the actual coefficient of permeability for Nevada sand with $D_r = 55\%$ is calculated to be $k = 5.8 \times 10^{-5}\ m/\sec$. As mentioned above, the prototype soil permeability is twice that of Nevada sand. Thus, the prototype permeability of the soil deposit in centrifuge experiment is equal to $11.6 \times 10^{-5}\ m/\sec$.

Initial saturation can have a significant effect on soil response. In fully saturated conditions, the pores are completely filled with water and the bulk stiffness of pore fluid is equal to bulk stiffness of water i.e. $K_f = 2 \times 10^6\ kPa$. Less than full saturation leads to a substantial decrease in the pore fluid (water + air) bulk stiffness. If the degree of saturation is slightly reduced, to say $S_r = 0.99$, the pore

fluid bulk stiffness will drop to $K_f = 1 \times 10^4 kPa$ at atmospheric pressure [38]. Change in fluid bulk stiffness affects the pore pressure build-up and settlement responses. Reduction of fluid bulk stiffness leads to slower pore pressure rise and somewhat larger amount of settlement. In addition to that, presence of air bubbles in pore void space can affect (reduce) permeability as well. In a centrifuge experiment, the degree of saturation can be evaluated by measuring compressional wave speed. Unfortunately, in the above mentioned experiment that is used for comparison with simulations, no such measurement was carried out and therefore, initial degree of saturation remains unknown. However, by comparing the rate of pore pressure development in numerical results with experimental records, it can be indirectly determined. An assumption of 100% saturation led to predictions of excess pore pressure rise that were significantly faster than those observed. Through a trial and error procedure, it was deduced that the fluid bulk stiffness of $K_f = 5.5 \times 10^4 kPa$ gives the best match with the experimental measurements. Considering the average pressure level in the centrifuge experiment, this bulk stiffness was determined to be equivalent to the initial saturation level of 98.8%.

Simulations were carried out in two load stages. First, a self weight loading stage was performed for both soil and steel plate. After reaching equilibrium for self weight, which will include proper evolution of elastic-plastic material (soil) with its stresses, strains, internal variables, the system is ready for second loading stage. In addition to that, main degrees of freedom (unknowns), solid skeleton displacements and pore fluid pressures, at the end of this first stage of loading, were then used as initial values for second stage of loading, comprising dynamic loading which would include seismic shaking and after that the dissipation of pore fluid excess pressures until hydrostatic conditions are reached.

7. Results and discussion

A number of simulations were performed using both variable permeability models (Equations (14) and (15)). Calibration of material parameters that control variable permeability (α, β_1, β_2, β_3, t_2 and

t_3) was performed by analyzing simulation results and comparing them with centrifuge test results. This was done for both models (Equations (14) and (15)). In addition to that, a sensitivity analysis was carried out to determine effect different parameters have on results and to improve calibration effort. Sensitivity analysis was performed for both models (Equations (14) and (15)) and an effort was made to find the best calibration for variable permeability material parameters. Moreover, both simulation results obtained using two models described above were then compared with results obtained by using so called "constant increased permeability coefficient" that is sometimes advocated as a simple remedy for variability of permeability during liquefaction [5, 12, 13].

7.1. Variable permeability using Model I (Eq. (14))

Calibration effort, which included sensitivity analysis, resulted in the following parameters for model I (Equation (14)):

$$\alpha = 20 \quad , \quad \beta_1 = 1.0 \quad , \quad \beta_2 = 8.9$$

Close inspection of Equation (14) reveals that, with $\alpha = 20$, the coefficient of permeability increases 20 times during liquefaction (when $r_u = 1$). This value is larger than what is reported by Arulanandan and Sybico [5] and Jafarzadeh and Yanagisawa [6]. However, this high value is consistent with average value reported by Balakrishnan [12] (peak value of 20 is equivalent with averaged value of 10). It is noted that the permeability coefficient is difficult to measure and large variations of measurement for (same) sand do exists. So, this peak value may alter due to the inaccuracy involved in the measurement of initial permeability value.

Using the calibrated values for parameters β_1 and β_2, the permeability coefficient obtained from Equation (14a) (in build-up phase) for a given value of r_u will be larger than the permeability coefficient from Equation (14c) (in dissipation phase). This reveals that the rate of drainage before onset of liquefaction is significantly higher than the rate of dissipation after liquefaction phase.

Above parameters were used in simulation and results for time histories of excess pore pressure ratio (r_u) at nodes P1 to P6, and vertical settlement at the soil surface are presented in Figures 10 and 11, together with experimental measurements. It is noted that both pore pressures and settlements are in good agreement with the experimental measurements.

The measured time histories of pore pressure ratio indicate a state of liquefaction or close to liquefaction at all levels. Liquefaction occurs first at the soil surface (transducer P5 and P6) and propagates downward. The results of the numerical modeling show that the liquefaction occurrence along the soil column has been predicted well.

The magnitude of the excess pore pressure is higher at the bottom, and is lower at the top, causing a pore pressure gradient which results in an upward flow. Due to this gradient, it is expected that the excess pore pressure at the bottom of the sand layer dissipates first. However, the measurements in the current centrifuge experiment show that the drainage is starting from the shallow depths. The main reason for the early drainage from shallow depths is the effect of steel plate used in centrifuge experiments. The steel plate provided a high vertical stress equivalent to 14 meters of submerged soil depth, but it can not create the same drainage condition that a 14 meters column of saturated sand does, hence a large excess pore pressure gradient developed near the surface which accelerated the dissipation rate at shallow depths. As can be observed in Figure 10, the simulation results confirm the issue of early drainage from shallow depths.

According to the experimental measurements, drainage at the middle and bottom of the soil column occurs a while after the end of shaking. The drainage sequence is from bottom to top. Although in the simulation results the drainage sequence starting from bottom to top is evident, the numerical modeling shows that drainage at the lower depths occurs just after the end of shaking. It seems that the predicted behavior matches with the concept of upward flow mentioned earlier, although this warrants further investigations.

The long term excess pore pressure distribution along the soil column at times 12 and 18 minutes is presented in Figure 12. As observed, the predicted amount of dissipation at shallow depths is more than experimental measurements. This may be because of partial prevention of surface drainage due to the existence of steel plate during the centrifuge experiment which results in the lower rate of dissipation at shallow depths. The obtained large value for parameter β_2 also indicates the low rate of dissipation after earthquake shaking.

7.2. Variable permeability using Model II (Eq. (15))

Sensitivity analysis on the parameters of Eq. (15) was performed by optimizing values for constants. It was found that the following values give the optimal agreement for both pore pressures and settlement:

$$\alpha = 20 \quad , \quad \beta_1 = 1.0 \quad , \quad \beta_3 = 10.0 \quad , \quad \Delta t_{peak} = 12\,\text{sec} \quad , \quad t_3 = 220\,\text{sec}$$

The results of simulation using Eq. (15) and the above parameters are almost exactly similar to the results presented in Figures 10 and 11 and are not presented again.

Parameters α and β_1 are equal to the calibrated values for Eq. (14) which shows the same permeability variation in the pore pressure build-up phase by two equations. As depicted in Figure 10, the numerical model using Eq. (14) shows a state of liquefaction at all depths of the soil column starting from 22 to 25 seconds and continues until the end of shaking at 35 seconds, i.e. the whole soil column is in a liquefied state for 10 to 13 seconds. This period coincides with the calibrated value for Δt_{peak} parameter. Therefore, both permeability functions predict almost the same values for permeability variation during pore pressure build-up and liquefaction phases. This is shown in Figure 13(a), where predicted values of permeability along the soil column are plotted at times 10, 20 and 30 seconds.

The values of predicted permeabilities along the soil column during dissipation phase at times 1, 2, and 3 minutes are shown in Figure 13(b). It should be emphasized that the permeability variation

predicted by Eq. (15) becomes nearly constant along the soil column during the dissipation phase because Eq. (15) is no longer a function of r_u. However, the value of permeability at each depth using Eq. (14) is determined based on the remaining pore pressure in that location, and so the predicted permeability becomes variable along the depth of a soil column. As observed in Figure 13(b), the coefficient of permeability returns back to its initial value at the time of about 3 minutes. At this time, the excess pore pressure ratio (r_u) along the soil column is in the range of 0.4 to 0.6. This indicates that the coefficient of permeability returns back to its initial value at approximately the middle of dissipation phase.

To demonstrate the effects of two different permeability equations on the pore pressure response in the dissipation phase, the long term excess pore pressure distributions along the soil column at times 1, 3, 6, and 12 minutes are presented in Figure 14. It is notable that despite the different permeabilities obtained from Eq. (14) and (15) (Figure 13(b)) at the beginning of dissipation phase, the values of excess pore pressure along the soil column are quite similar. This indicates that the average values of the predicted permeabilities along the soil column and over the time are almost identical. Therefore, application of Eq. (15) does not seem to introduce much improvement over Eq. (14).

Consequently, assuming a direct relationship between the permeability coefficient and r_u during build-up, liquefaction, and dissipation phases, as explained by Eqs. (14a) to (14c), enables fairly accurate simulation the actual phenomenon and can therefore be proposed for liquefaction modeling.

7.3. "Constant increased permeability" method

In order to test usually made assumption of constant increase in permeability during pore pressure buildup, liquefaction and dissipation, two sets of results are presented. Namely, numerical simulations with constant permeability values of $k_{initial}$ and $10.5k_{initial}$ along with the simulation results with variable permeability are presented in Figures 15 and 16.

As expected, the amount of settlement in the numerical analysis with a permeability value of $k_{initial}$ is smaller than the measured value. As shown, in order to simulate the measured settlement the permeability coefficient should be (constantly) increased to 10.5 times of its initial value. However, this increased constant permeability has a negative effect on the pore pressure response. As observed in Figure 15, predicted excess pore pressure at shallow depths is considerably lower than the measured value and the liquefaction state can not be identified clearly. However, the predicted pore pressures and liquefaction state using variable permeability relation demonstrate good match with the experimental measurements. So, it is concluded that the assumption of "constant increased permeability" can not capture all features of the soil response in liquefaction modeling. In addition to that, such an assumption may erroneously predict no liquefaction at certain depths.

8. Summary and conclusion

In this paper it was shown that proper consideration of the variable permeability coefficient, in addition to use of a suitable constitutive model for simulating contraction behavior of sand are the key ingredients in liquefaction modeling. By employing a suitable constitutive model and taking the variability of permeability into account, it becomes possible to obtain good results for pore pressure variation in the soil mass and also predict a reliable value for the settlement.

In this study, by employing of a well calibrated critical state two-surface plasticity model for simulation of soil skeleton response, the focus of attention was on the variation of permeability. New relationships for evaluating the variation of the coefficient of permeability during the liquefaction process were proposed. The proposed relationships were implemented in a simulation program that is based on parts of OpenSees framework, UCD computational Geomechanics tools (elements, material models, constitutive algorithms) and solvers from UmfPack library. Numerical simulations were performed to saturated sand soils subjected to earthquake loading in centrifuge experiment. By

comparing the numerical results with centrifuge experiment records, the suitable relationship was identified and its constants were calibrated. Proper modeling of models analysis showed that, even though centrifuge experiments had some deficiencies in modeling of prototype behavior, proper choice of numerical analysis parameters effectively resolves such deficiencies for prototype scale numerical modeling. The main findings of this investigation can be summarized as follows:

1. The variation of permeability coefficient during liquefaction can be expressed as a function of excess pore pressure ratio. Comparison of numerical simulation results and the centrifuge experiment measurements indicate that there is a direct relationship between the permeability coefficient and excess pore pressure ratio during build-up, liquefaction and dissipation phases.
2. The coefficient of permeability increases significantly during seismic excitation and excess pore pressure generation. In the current study, its peak value during the initial stages of liquefaction reaches almost 20 times initial permeability. From the practical viewpoint, the permeability coefficient is difficult to measure. So, this peak value may alter due to the inaccuracy involved in the measurement of initial permeability value.
3. Rate of drainage of pore water pressure/volume before onset of liquefaction where generation of pore pressure and drainage of pore water occur simultaneously, is significantly higher than the rate of dissipation after ending of liquefaction where the dissipation is the dominant mechanism.

Although the proposed model for variation of permeability during stages of liquefaction modeling seems very promising, applicability of developed models to different conditions might require further investigation.

Acknowledgements

The authors would like to sincerely appreciate Professor L. Gonzalez for kindly providing digital data of the centrifuge experiment. The contribution of Mr. N. Fotovat in the programming features is gratefully acknowledged.

References

1. Ishihara K. Review of the predictions for Model 1 in the VELACS program. In: Arulanandan K, Scott RF (eds.), Verification of Numerical Procedures for the Analysis of Soil Liquefaction Problems, A.A. Balkema, Rotterdam, 1994: 1353-1368.
2. Tokimatsu K, Seed HG. Evaluation of settlements in sands due to earthquake shaking. Journal of Geotechnical Engineering, ASCE 1987; **113**(8): 861-878.
3. Schofield AN. Dynamic and earthquake centrifuge geotechnical modeling. In: Proceeding of International Conference on Recent Advances in Geotechnical Earthquake Engineering and Soil Dynamics, University of Missouri-Rolla, Mo., 1981: 1081-1100.
4. Hushmand B, Crouse CB, Martin GR, Scott RF. Site response and liquefaction studies involving the centrifuge. In: Proceeding of 3rd International Conference on Soil Dynamics and Earthquake Engineering, Elsevier, 1987: 3-24.
5. Arulanandan K, Sybico JJr. Post-liquefaction settlement of sand. In: Proceeding of the Wroth Memorial Symposium, Oxford University, England, 1992.
6. Jafarzadeh F, Yanagisawa E. Settlement of sand models under unidirectional shaking. In: Ishihara K (ed.), First International Conference on Earthquake Geotechnical Engineering, IS-Tokyo, 1995: 693-698.
7. Carman PC. Flow of gases through porous media. New York: Academic Press, 1956.
8. Arulanandan K, Scott RF. Verification of numerical procedures for the analysis of soil liquefaction problems. A.A. Balkema, Rotterdam, 1993.
9. Yang Z, Elgamal A. Influence of permeability on liquefaction-induced shear deformation. Journal of Engineering Mechanics 2002; **128**(7): 720-729.
10. Zienkiewicz OC, Xie YM. Analysis of lower San Fernando dam failure under earthquake. Dam Engineering 1991; **2**(4): 307-322.

11. Yoshida N, Finn WDL. Simulation of liquefaction beneath an impermeable surface layer. Soil Dynamics and Earthquake Engineering 2000; **19**: 333-338.
12. Balakrishnan A. Liquefaction remediation at a bridge site. PhD Dissertation, University of California, Davis, 2000.
13. Taiebat M, Shahir H, Pak A. Study of pore pressure variation during liquefaction using two constitutive models for sand. Soil Dynamics and Earthquake Engineering 2007; **27**: 60-72.
14. Manzari MT, Arulanandan K. Numerical predictions for Model No. 1. In: Arulanandan K, Scott RF (eds.), Verification of Numerical Procedures for the Analysis of Soil Liquefaction Problems, A.A. Balkema, Rotterdam, 1993: 179-185.
15. Oberkampf WL, Trucano TG, Hirsch C. Verification, validation and predictive capability in computational engineering and physics. In: Laurel MD (ed.), Proceedings of the Foundations for Verification and Validation on the 21st Century Workshop, Johns Hopkins University/Applied Physics Laboratory: Baltimore, MD, 2002: 1–74.
16. Taboada VM, Dobry R. Experimental results of model No. 1 at RPI. In: Arulanandan K, Scott RF (eds.), Verification of Numerical Procedures for the Analysis of Soil Liquefaction Problems, A.A. Balkema, Rotterdam, 1993: 3-18.
17. McKenna FT. Object oriented finite element programming: framework for analysis, algorithms and parallel computing. Ph.D. Thesis, University of California, Berkeley, 1997.
18. Jeremic B, Sture S. Tensor data objects in finite element programming. International Journal for Numerical Methods in Engineering 1998; **41**:113–126.
19. Jeremic B, Yang Z. Template elastic–plastic computations in geomechanics. International Journal for Numerical and Analytical Methods in Geomechanics 2002; **26**(14): 1407–1427.
20. Davis TA, Duff IS. A combined unifrontal/multifrontal method for unsymmetric sparse matrices. Technical Report TR97-016 (UF) and TR-97-046 (RAL), University of Florida and Rutherford Appleton Laboratory, 1997.

21. Jeremic B. Development of geotechnical capabilities in OpenSees. Report No. PEER2001/12, Pacific Earthquake Engineering Research Center, 2001.
22. Dafalias YF, Manzari MT. Simple plasticity sand model accounting for fabric change effects. Journal of Engineering Mechanics 2004; **130**(6): 622-634.
23. Manzari MT, Dafalias YF. A critical state two-surface plasticity model for sands. Geotechnique 1997; **47**(2): 255-272.
24. Dafalias YF. Bounding surface plasticity, I: Mathematical foundation and hypoplasticity. Journal of Engineering Mechanics 1986; **112**(9): 966-987.
25. Schofield AN, Wroth CP. Critical state soil mechanics. McGraw-Hill, New York, 1968.
26. Taiebat M, Dafalias YF. SANISAND: simple anisotropic and plasticity model. International Journal for Numerical and Analytical Methods in Geomechanics 2008; **32**(8): 915-948.
27. Rowe PW. The stress-dilatancy relation for static equilibrium of an assembly of particles in contact. In: Proc. Roy. Soc., Series A, 1962; **269**: 500-527.
28. Ishihara K, Tatsuoka F, Yasuda S. Undrained deformation and liquefaction of sand under cyclic stresses. Soils and Foundations 1975; **15**(1): 29-44.
29. Wood DM, Belkheir K, Liu DF. Strain softening and state parameters for sand modeling. Geotechnique 1994; **44**(2): 335-339.
30. Been K, Jefferies MG. A state parameter for sands. Geotechnique 1985; **35**(2): 99-112.
31. Li XS, Wang Y. Linear representation of steady-state line for sand. Journal of Geotechnical and Geoenvironmental Engineering 1998; **124**(12): 1215-1217.
32. Arulmoli K, Muraleetharan KK, Hossain MM, Fruth LS. VELACS Laboratory testing program: Soil data report. The Earth Technology Corporation, 1992.
33. Hazen A. Discussion of: Dams on sand foundation, by Koenig AC. Transaction ASCE 1911; **73**: 199.

34. Samarasinghe AM, Huang YH, Drnevich VP. Permeability and consolidation of normally consolidated soils. Journal of Geotechnical Engineering Division, ASCE 1982; **108**: 835-850.
35. Gonzalez L, Abdoun T, Sharp MK. Modeling of seismically induced liquefaction under high confining stress. International Journal of Physical Modeling in Geotechnics 2002; **2**(3): 1-15.
36. Wood DM. Geotechnical Modeling. Spoon Press, 2004.
37. Taylor RN. Geotechnical centrifuge technology. Blackie Academic & Professional, 1995.
38. Fredlund DG, Rahardjo H. Soil mechanics for unsaturated soils. Wiley-Interscience, 1993.

Tables Caption:

Table 1: Material parameters of the critical state two-surface plasticity model for Nevada sand

Table 2: Permeability coefficient of Nevada sand [32]

Table 1: Material parameters of the critical state two-surface plasticity model for Nevada sand

Constant	Variable	Value
Elasticity	G_0	150
	ν	0.05
Critical state	M	1.14
	c	0.78
	λ_c	0.027
	e_0	0.83
	ξ	0.45
Yield surface	m	0.02
Plastic modulus	h_0	9.7
	c_h	1.02
	n^b	2.56
Dilatancy	A_0	0.81
	n^d	1.05
Fabric-dilatancy tensor	$z_{\max}$	5
	c_z	800

Table 2: Permeability coefficient of Nevada sand [32]

Relative density (%)	Coefficient of permeability (m/sec)
40	6.6×10^{-5}
60	5.6×10^{-5}
91	2.3×10^{-5}

Figures Caption:

Figure 1: (a) Permeability function used by Manzari and Arulanandan [14] (b) Measured excess pore pressure ratios in centrifuge experiment [16]

Figure 2: Schematic representation of the two-surface model in the π-plane [22]

Figure 3: Simulation of three drained constant- p tests on Nevada sand with $D_r \approx 40\%$

Figure 4: Simulation of three drained constant- p tests on Nevada sand with $D_r \approx 60\%$

Figure 5: Simulation of an undrained triaxial test on Nevada sand with $D_r \approx 40\%$

Figure 6: Simulation of an undrained cyclic triaxial test on Nevada sand with $D_r \approx 40\%$

Figure 7: Schematic view of the proposed permeability functions

Figure 8: (a) Setup and instrumentations of the centrifuge experiment [35] (b) Finite element mesh and boundary conditions

Figure 9: Prototype time history of input motion [35]

Figure 10: Predicted time histories of pore pressure ratio using Eq. (14)

Figure 11: Predicted time history of settlement using Eq. (14)

Figure 12: Predicted distribution of long-term excess pore pressures along the soil column using Eq. (14)

Figure 13: Predicted permeability variations along the soil column (a) during build-up and liquefaction (b) during dissipation

Figure 14: Comparison of predicted long-term excess pore pressures by Eqs. (14) and (15)

Figure 15: Predicted time histories of pore pressure ratio with constant and variable permeability assumptions

Figure 16: Predicted time histories of settlement with constant and variable permeability assumptions

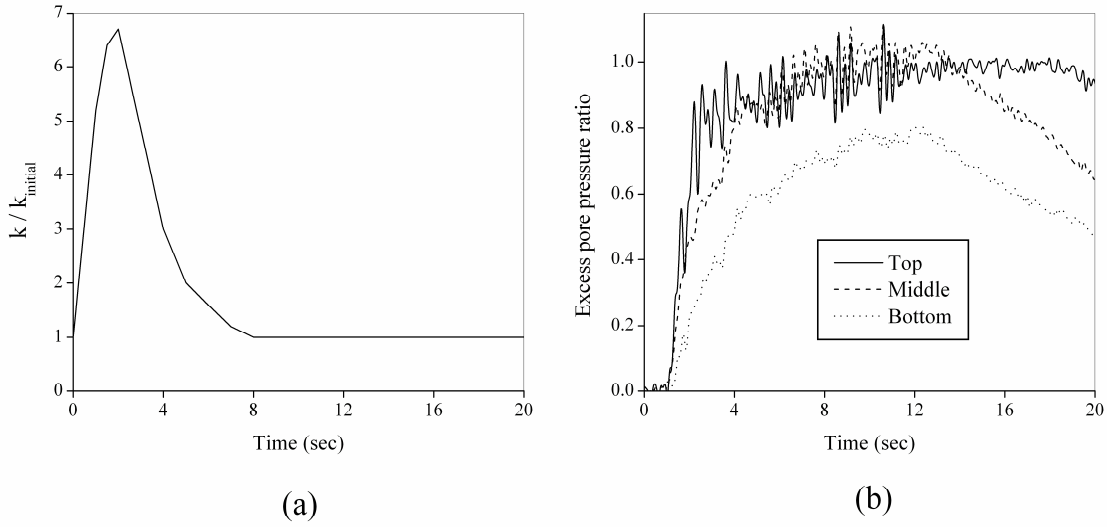

Figure 1: (a) Permeability function used by Manzari and Arulanandan [14]

(b) Measured excess pore pressure ratios in centrifuge experiment [16]

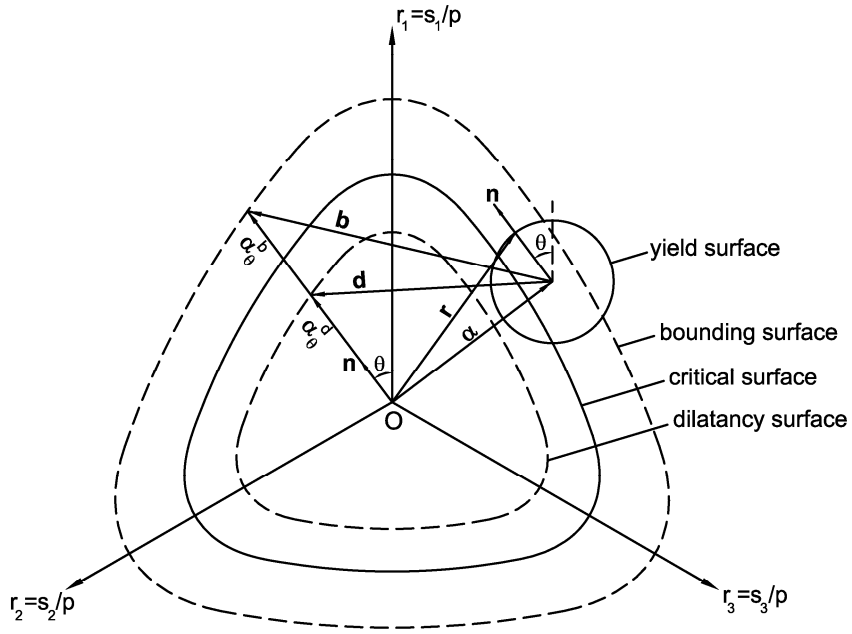

Figure 2: Schematic representation of the two-surface model in the π-plane [22]

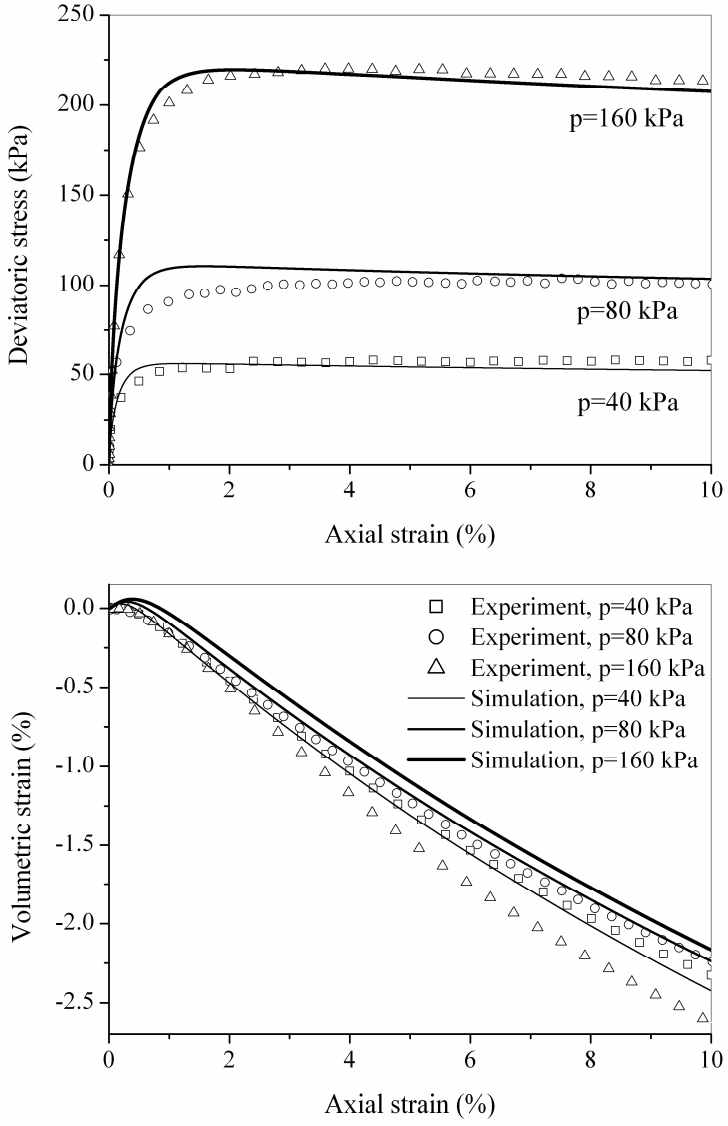

Figure 3: Simulation of three drained constant- p tests on Nevada sand with $D_r \approx 40\%$

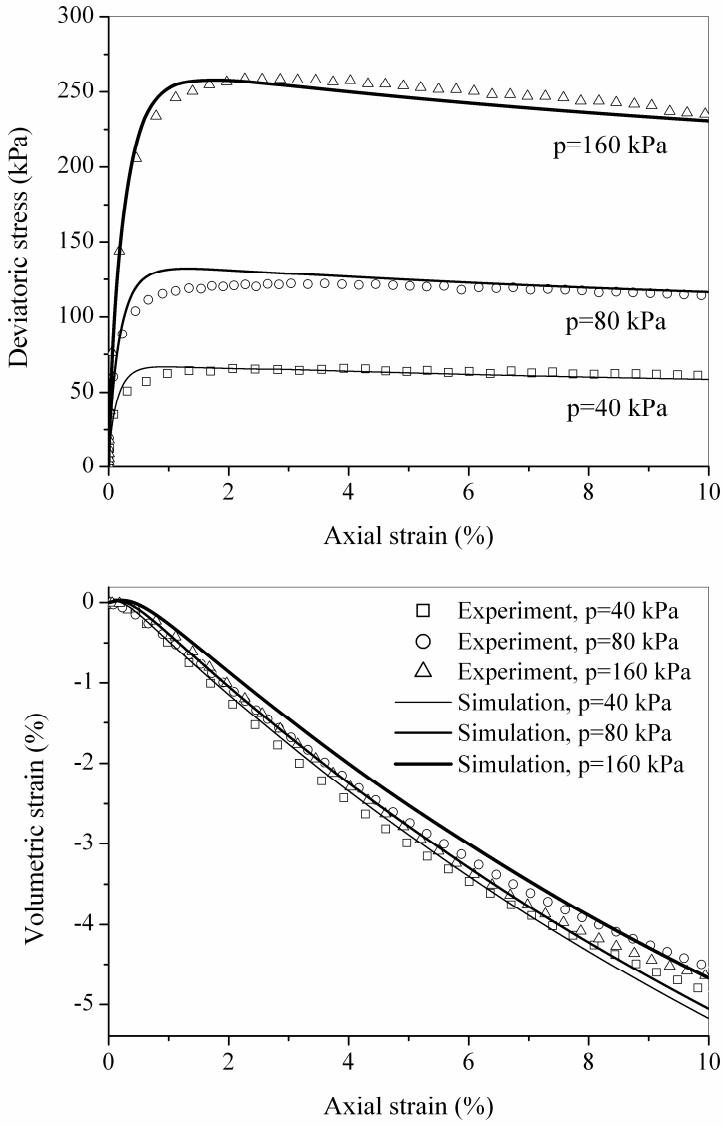

Figure 4: Simulation of three drained constant- p tests on Nevada sand with $D_r \approx 60\%$

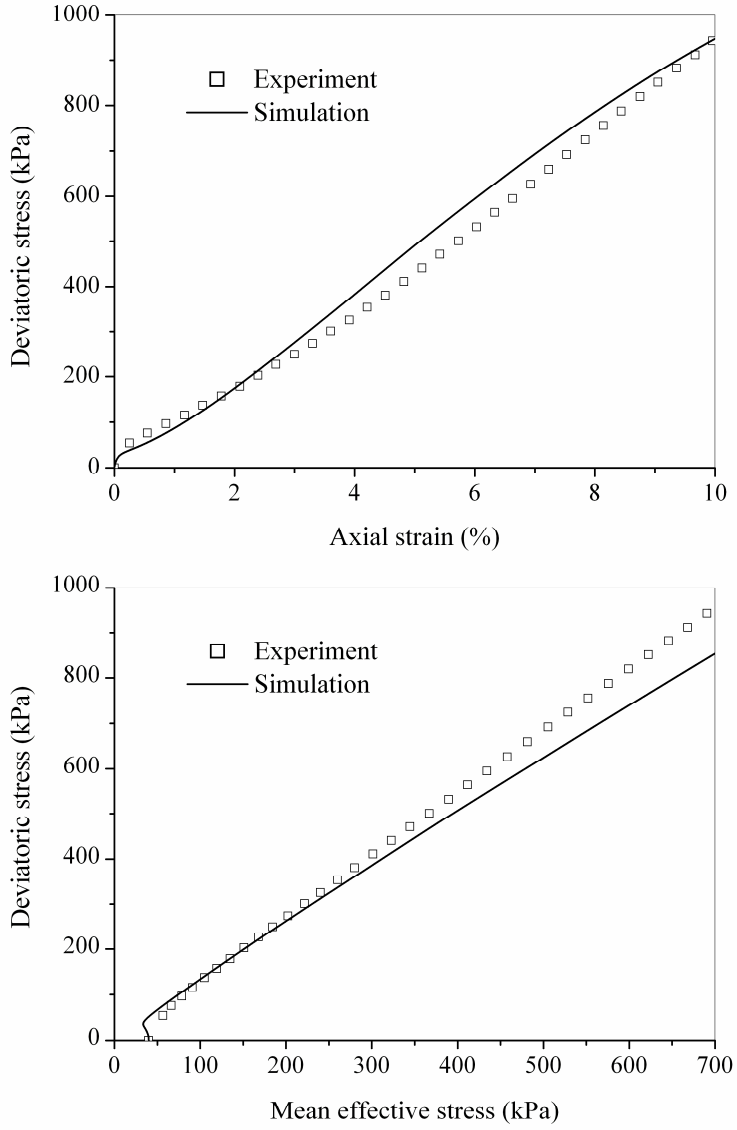

Figure 5: Simulation of an undrained triaxial test on Nevada sand with $D_r \approx 40\%$

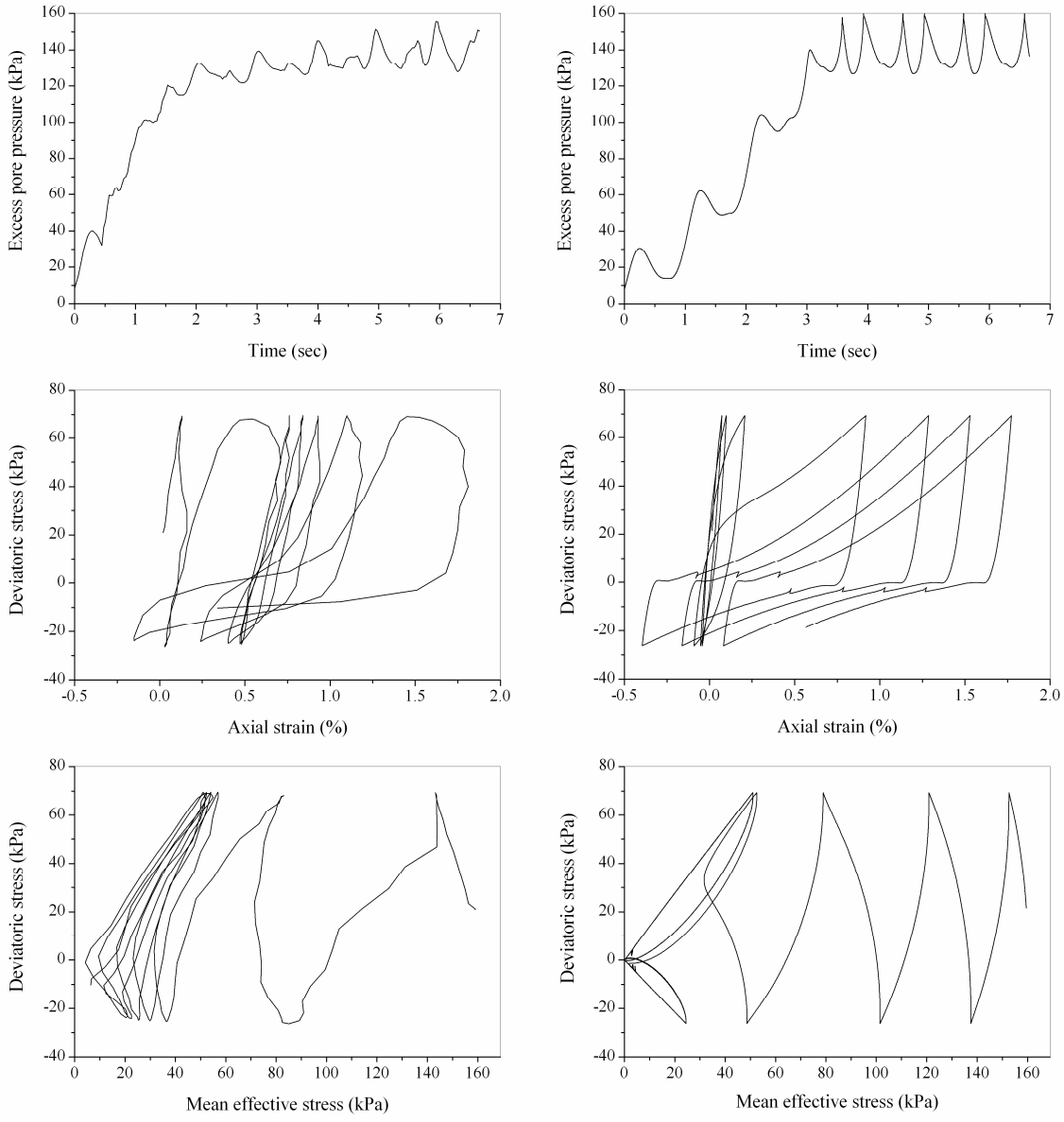

(a) Experiment (b) Simulation

Figure 6: Simulation of an undrained cyclic triaxial test on Nevada sand with $D_r \approx 40\%$

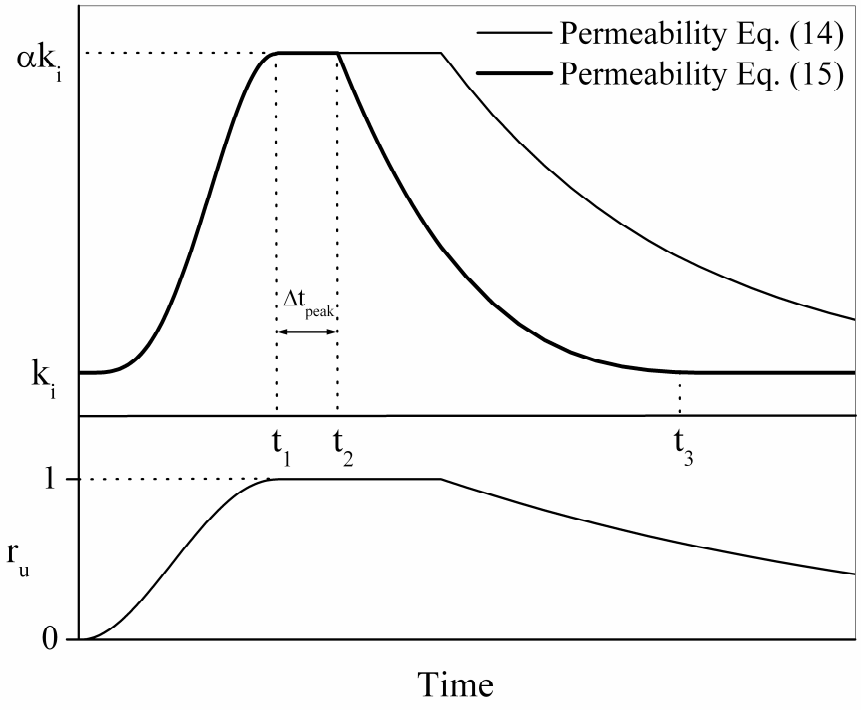

Figure 7: Schematic view of the proposed permeability functions

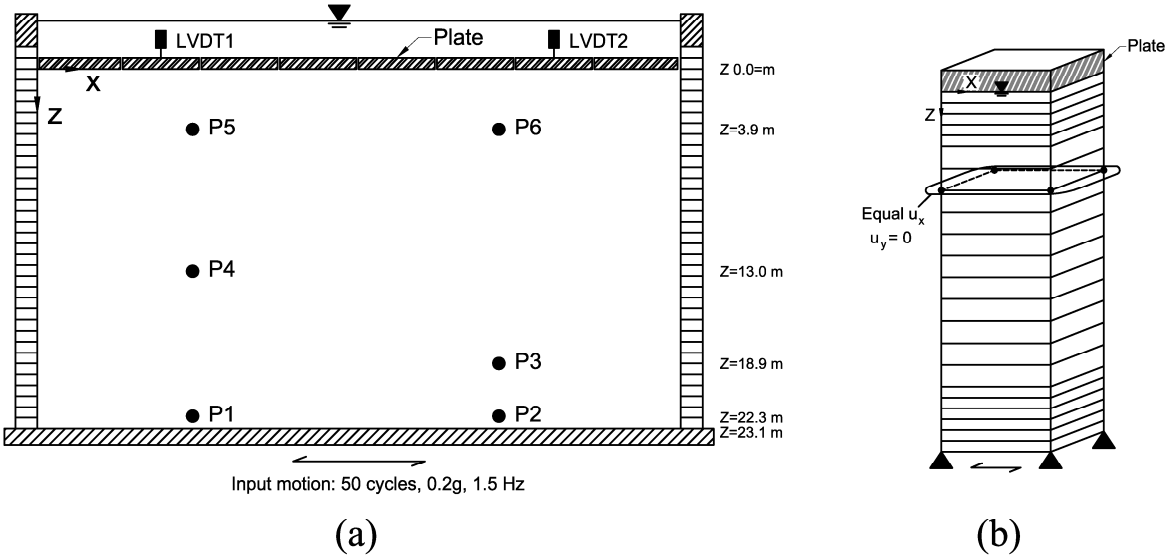

Figure 8: (a) Setup and instrumentations of the centrifuge experiment [35]

(b) Finite element mesh and boundary conditions

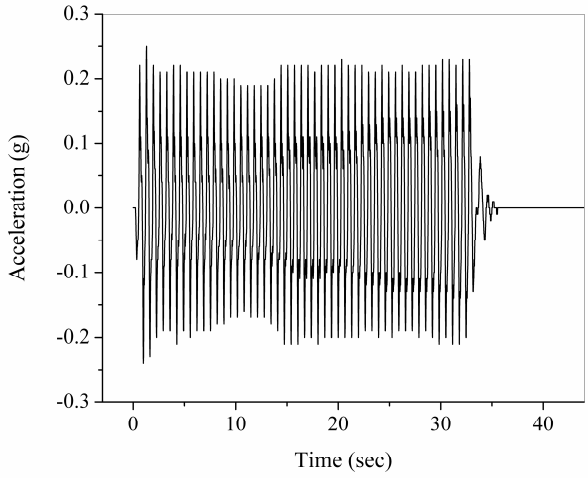

Figure 9: Prototype time history of input motion [35]

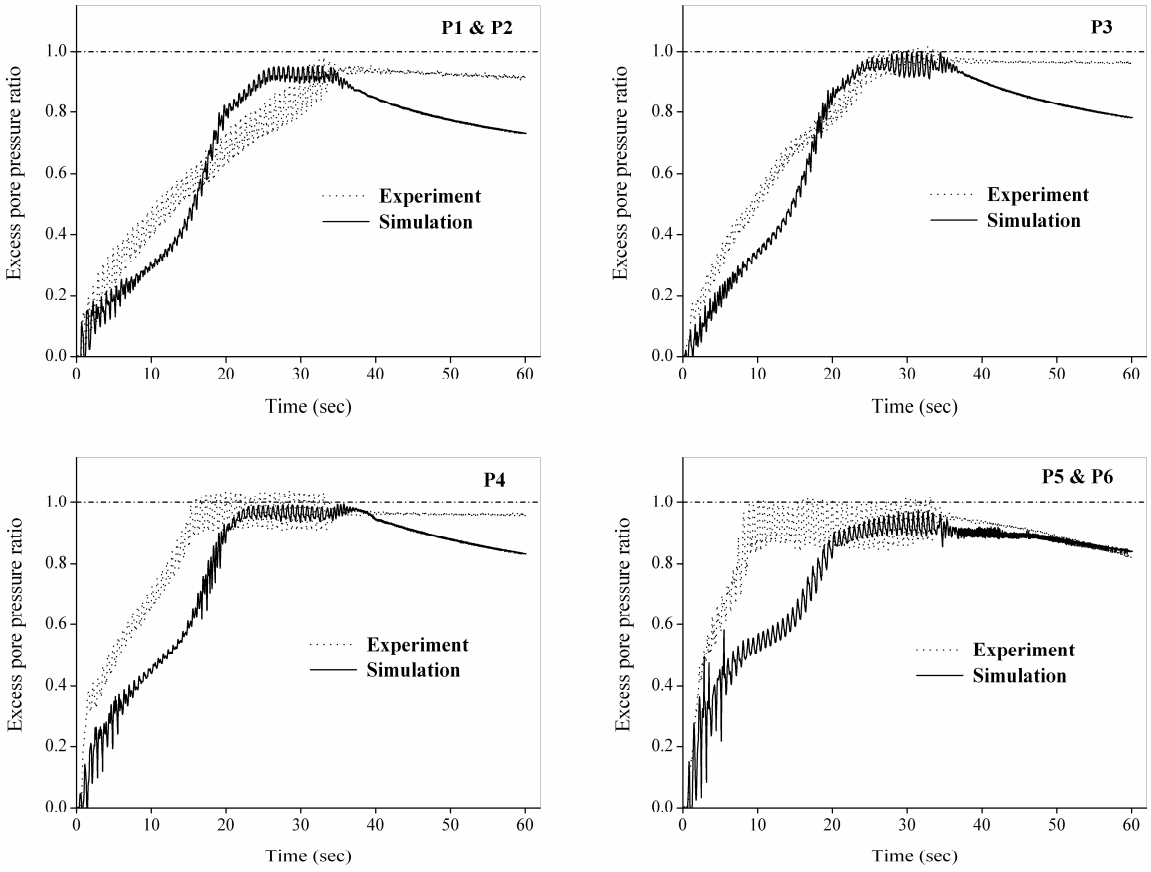

Figure 10: Predicted time histories of pore pressure ratio using Eq. (14)

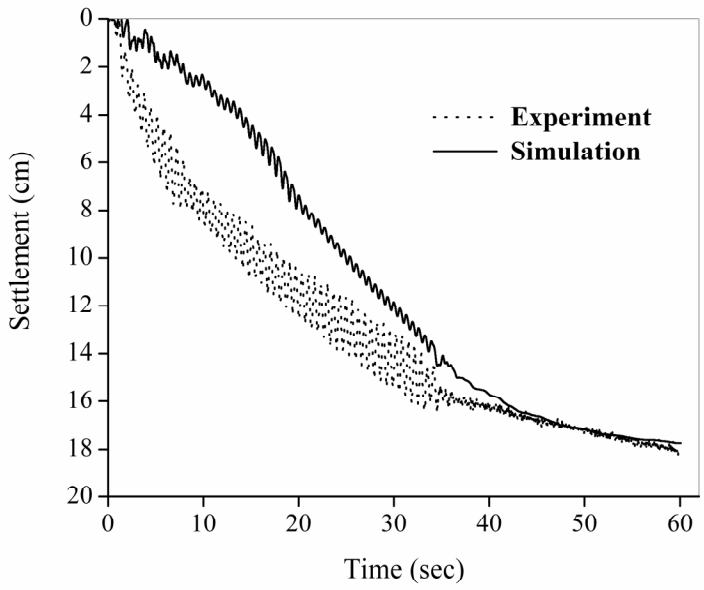

Figure 11: Predicted time history of settlement using Eq. (14)

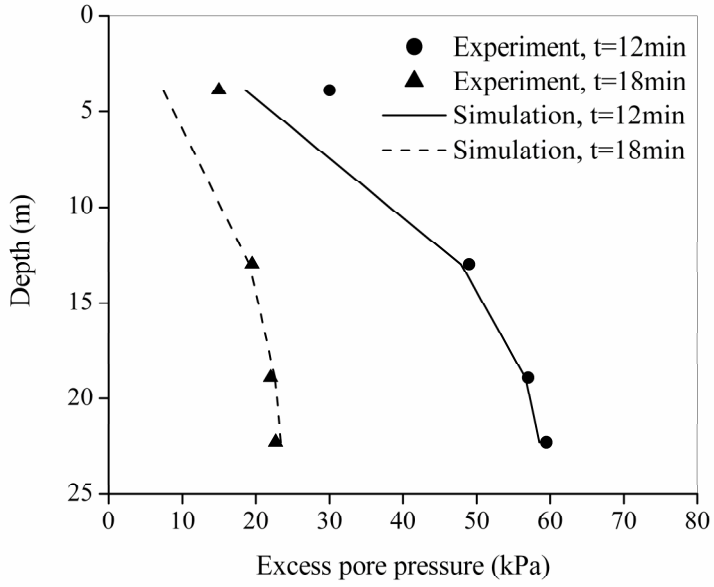

Figure 12: Predicted distribution of long-term excess pore pressures along the soil column using Eq. (14)

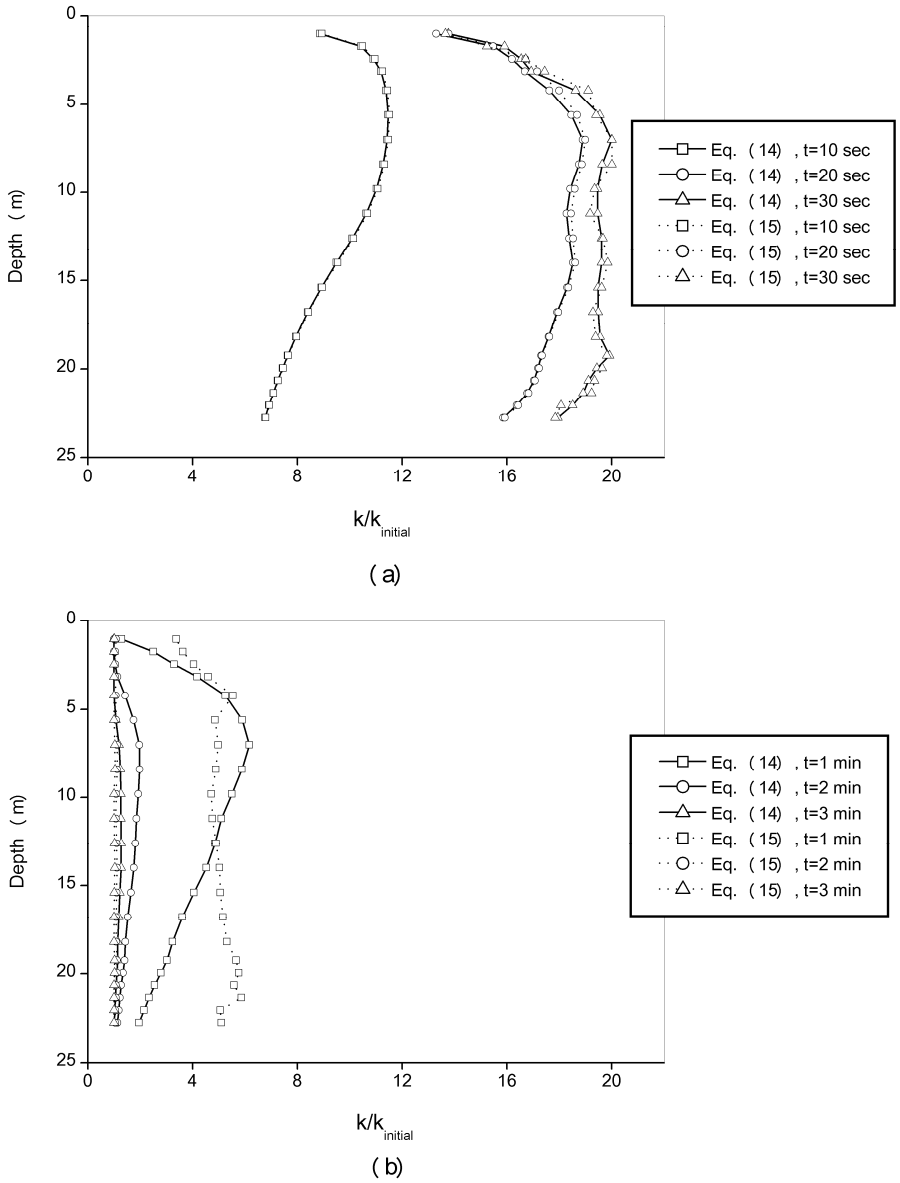

Figure 13: Predicted permeability variations along the soil column (a) during build-up and liquefaction (b) during dissipation

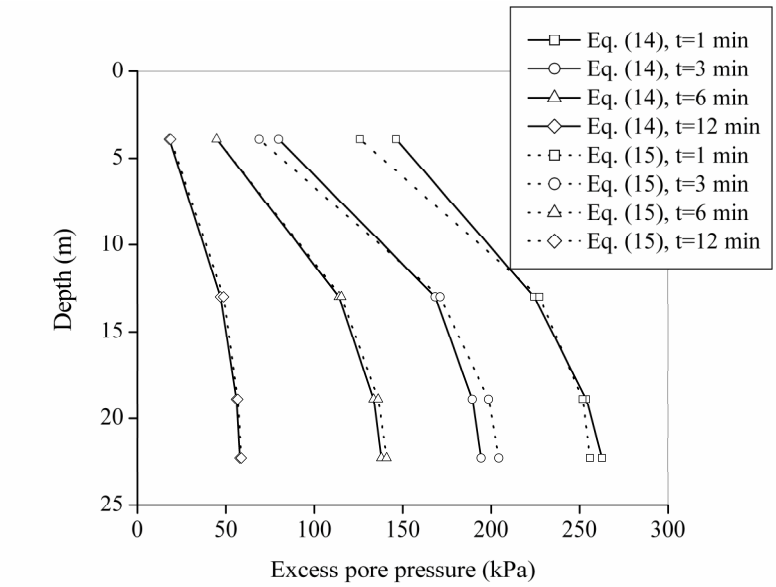

Figure 14: Comparison of predicted long-term excess pore pressures by Eqs. (14) and (15)

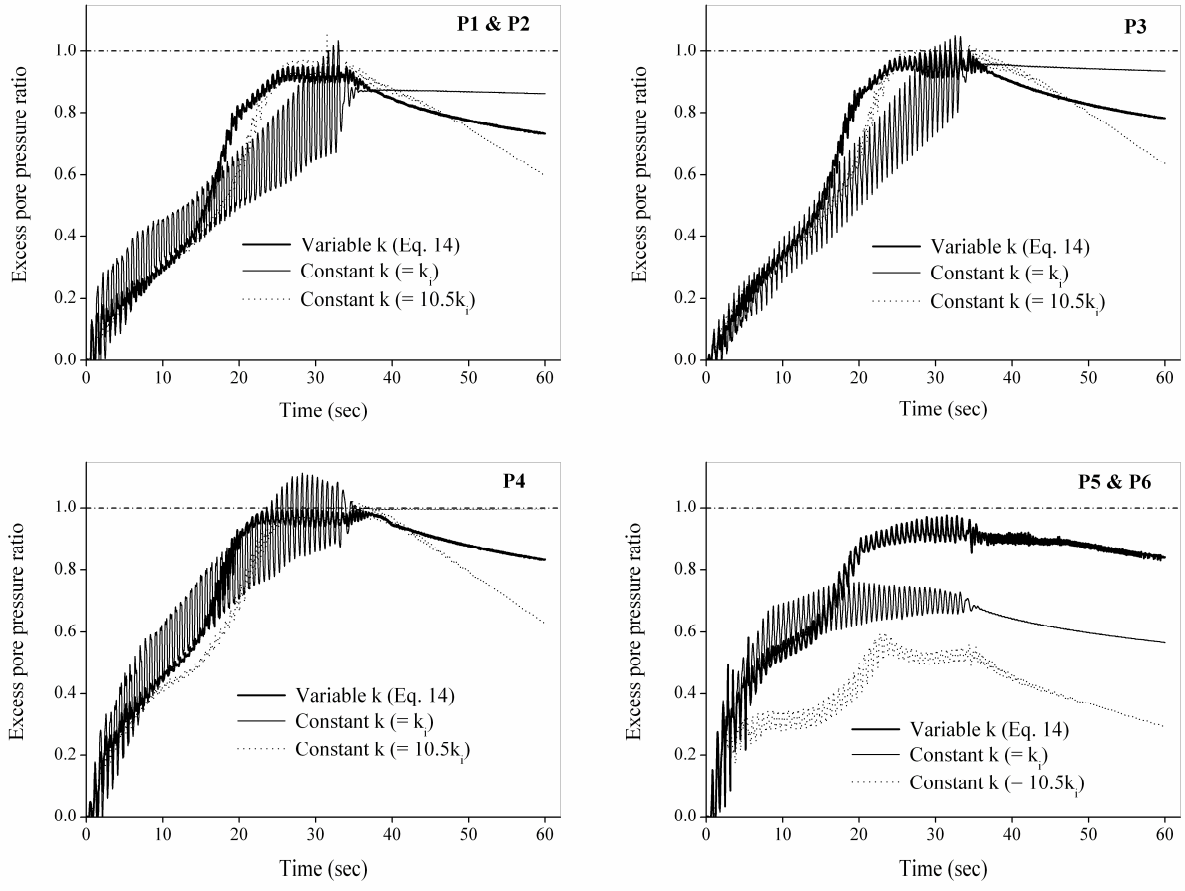

Figure 15: Predicted time histories of pore pressure ratio with constant and variable permeability assumptions

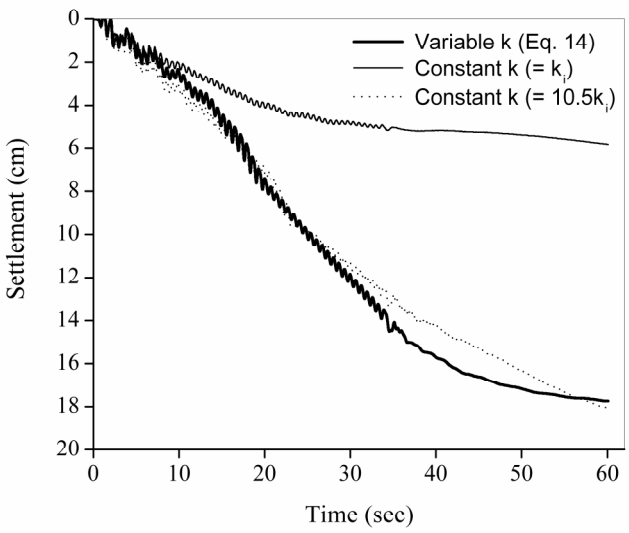

Figure 16: Predicted time histories of settlement with constant and variable permeability assumptions